Int. J. Electrochem. Sci., 17 **(2022)** Article Number: 220818, doi: 10.20964/2022.08.16

International Journal of
ELECTROCHEMICAL
SCIENCE
www.electrochemsci.org

Effects of Heating Rate on Austenitic Transformation and Corrosion Property of High Chromium Ferritic/Martensitic Steel

Xuan Wang[1], *Jianguo Chen*[2 *], *Yong Guo*[1], *Weifei Niu*[1**]

[1] Key Laboratory of Digital Twin Generic Technology in Special Equipment for State Market Regulation, Tianjin Special Equipment Inspection Institute, Tianjin 300192, PR China;
[2] The 18th Research Institute of China Electronics Technology Group Corporation, Tianjin 300384, PR China;
[*]E-mail: jianguo_chen123@163.com (J. Chen), nwfei@163.com (W. Niu)

Received: 4 April 2022 / *Accepted:* 18 May 2022 / *Published:* 4 July 2022

The effect of heating rate on austenitic transformation and corrosion resistance of the high Chromium (Cr) ferritic/martensitic steel was studied. The grain size was observed by optical microscope (OM), the distribution of second-phases was observed by transmission electron microscope (TEM), and the thickness and phase composition of corrosion products were analyzed by scanning electron microscope (SEM) and X-ray diffraction (XRD), respectively. The results show that the heating rate can affect the austenitic transformation and corrosion resistance of the high Cr ferritic/martensitic steel. As the heating rate increases, the austenitic transformation time of the steel is suppressed, and the grain size of the steel decreases and the number of second-phases increases. Electrochemical polarization curves confirmed that with the increase of heating rate, the corrosion potential of steel sample decreased and the corrosion current increased, which indicates that the corrosion resistance of the high Cr ferritic/martensitic steel was deteriorated. In addition, there was no significant difference in the phase composition of the corrosion products after the immersion test. The thickness of corrosion products measured by SEM was in consistent with the results of electrochemical polarization curves.

Keywords: High Cr ferritic/martensitic steel; Austenite phase transformation; Carbide; Electrochemical polarization curves

1. INTRODUCTION

Compared with austenitic steels, high Chromium (Cr) ferritic/martensitic steels are considered as an important structural material for the main steam pipe with large-diameter and thick-walled in ultra-super critical (USC) thermal power plants, due to their lower price, lower thermal expansion coefficient, better creep resistance and higher thermal conductivity [1-3]. Austenitizing process is the first link in the heat treatment process of metallic materials, and it is extremely critical to the heat treatment efficiency and final microstructure and properties of materials in practical engineering [4,5]. During the austenitizing process, the grain size of austenite and the content of alloying elements dissolved in austenite will change, which greatly affects the microstructure and mechanical properties of the steel [6,7]. Grain size is an important factor in determining the strength and toughness of the metallic materials [8-10]. In steels, the austenitic grain size is a microstructural parameter that must be tightly controlled during hot working operations (such as hot rolling) and heat treatments, as well as in the heat-affected zone (HAZ) of welds. The austenitic grain produced by these thermal or thermomechanical processes provides the initial conditions for the subsequent phase transformation during cooling, which affects the final microstructure and mechanical properties of the steel [11-13]. For example, when the heat-affected zone undergoes a rapid thermal cycling and the peak temperature is high during welding, especially the large austenitic grain in the coarse-grained zone close to the fusion zone may reduce the weld toughness [14-18]. It also affects the vulnerability of welds cold and reheat cracks. Furthermore, the grain growth in the HAZ affects the grain size in the weld metal, in which the grains grow epitaxially from the HAZ. The diffusion and solid solution of alloying elements in the austenitizing process can lead to the change of austenitizing degree, relevant phases content and lattice parameters, thereby altering the microstructure and properties of the materials [19,20]. Therefore, the study of austenitizing process of steel materials has important theoretical and practical significance for controlling austenitic microstructure.

At present, the research on austenitization of high Cr ferritic/martensitic steels has mainly focused on the relationship between microstructure and mechanical properties. There are few reports on the corrosion performance. Corrosion is the most common failure mode for engineering materials [21], and clarifying its failure mechanism is extremely critical for the application of high Cr ferritic/martensitic steels. Therefore, the effect of austenitizing on the corrosion properties of the steel should be studied.

In this paper, the effect of heating rate on the austenitic transformation and corrosion performance of high Cr ferritic/martensitic steel is systematically studied through austenitic transformation analysis, microstructure observation and electrochemical polarization curve, which can provide guidance for the heat treatment of ferritic/martensitic steel in practical engineering.

2. MATERIALS AND EXPERIMENT METHODS

2.1 Specimens preparation

The high Cr ferritic/martensitic steel was casted into a 28 kg ingot in a vacuum induction furnace, melted twice to ensure its high uniformity, and then forged into a cylindrical bar with a height of 350 mm and a diameter of 120 mm. The chemical composition of the experimental steel is shown in Table 1. The microstructure of the steel is martensite with a small amount of δ-ferrite, and its grain size is slightly uneven, as shown in Fig. 1.

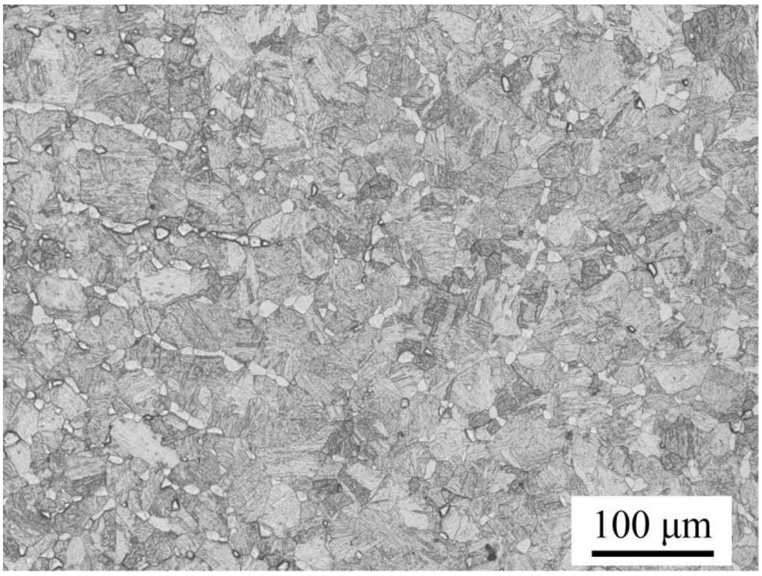

Figure 1. Optical micrographs of the original high Cr ferritic/martensitic steel.

Table 1. Chemical composition of the high Cr ferritic/martensitic steel in wt.%

C	Cr	W	Mn	Si	V	Ta	Fe
0.04	8.93	1.72	0.44	0.04	0.22	0.07	Bal.

Fig. 2 shows the flow-process diagram of the heat treatment experiment for the high Cr ferritic/martensitic steel samples. The square specimens with length of 10 mm, width of 10 mm and height of 10 mm were cut from the steel bar by wire cutting method, and the austenitizing heat treatment test was carried out on a Gleeble-3500 thermal simulator. The specific test parameters are as follows: the steel blocks were heated to 1050 ^{o}C at the heating rates of 20 ^{o}C/min, 100 ^{o}C/min, 500 ^{o}C/min and 1000 ^{o}C/min for 10 min, respectively, and then air cooling to room temperature. The thermal expansion curve is used to characterize the phase transformation information of steel block. This method has been widely used in the analysis of phase transformation of metallic materials [22-25]. The basic principle is that when the phase transformation of metallic materials occurs, the change in the crystal structure will lead to the change of material volume, which is macroscopically manifested as the expansion or compression of the sample.

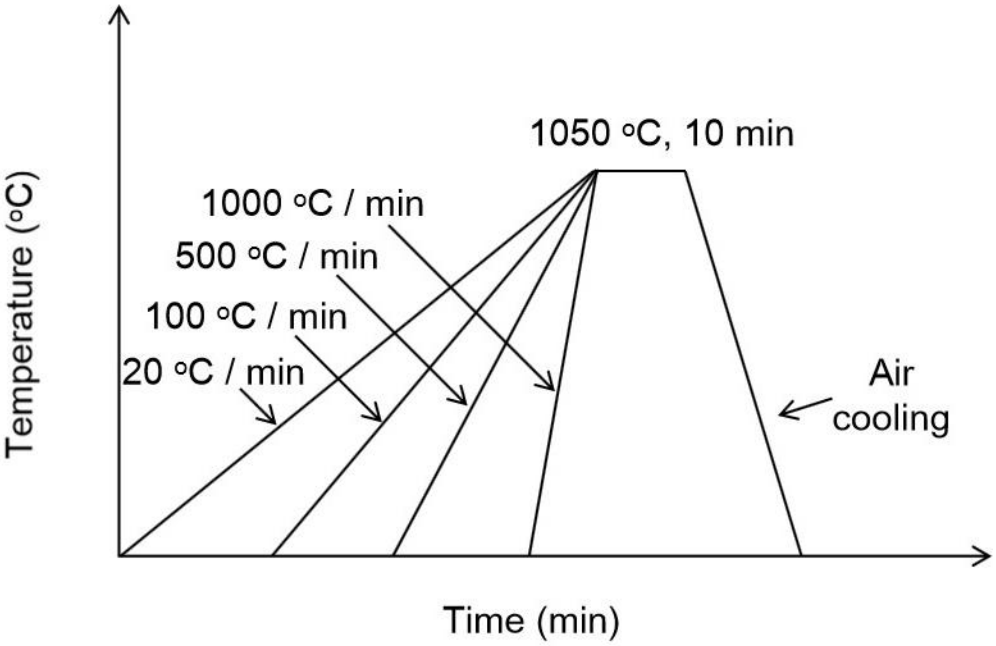

Figure 2. Flow-process diagram of the heat treatment experiment for the high Cr ferritic/martensitic steel samples.

2.2 Microstructure analysis

The microstructure of the high Cr ferritic/martensitic steel samples after thermal simulation experiment was observed by optical microscopy (OM). After the thermal simulation experiment, the samples were sequentially inlaid, ground, polished and etched. Saturated picric acid solution etching method was used to etch the microstructure of the samples. The detailed method is to place the polished metallographic samples in a saturated picric acid solution at 70 °C for 3 minutes, then wash the etched samples with alcohol, and finally observe the microstructure of the samples using Leica DMI 5000m OM. The formula of picric acid solution is 2 g picric acid + 2 ml abluent + 100 ml water. The linear intercept method was used to measure the prior austenite grain size of the steels in three different directions [26].

The distribution of second-phases was observed by transmission electron microscopy (TEM), and the type of second-phases was identified by energy dispersive spectrometer (EDS). The morphology, size and distribution of second-phase particles were observed by the carbon extraction replica technology owing to the blurring of second-phase phases in steel caused by diffraction contrast in metal foil. After deep etching and carbon coating on the sample surfaces, the surfaces were lightly scored into squares with a side length of 2 mm, and then the bulk replicas were liberated in the mixed solution of hydrochloric acid and copper chloride, and finally float the replicas out of ethanol and water.

2.3 Electrochemical measurements

Corrosion resistance of the high Cr ferritic/martensitic steel samples treated under different heating rates was studied by electrochemical polarization curves test. The electrochemical measurement was performed on a PARSTAT 4000A electrochemical workstation, which has three electrodes, i.e., a saturated calomel reference electrode, a platinum counter electrode and a working electrode made of the samples. The polarization curves of the high Cr ferritic/martensitic steel samples obtained at different heating rates were measured in 3.5 wt.% NaCl solution at room temperature. The scan rate was maintained at 0.4 mV/s during the electrochemical polarization curves test. The superficial area of the electrochemical testing samples is 1 cm^2.

2.4 Corrosion test and corrosion product analysis

The high Cr ferritic/martensitic steel samples obtained at different heating rates were immersed in 3.5% NaCl solution at room temperature for 30 days. After immersion experiment, the phase composition of the corrosion products was determined by Rigaku SmartLab-SE X-ray diffractometer (XRD) with CuKα radiation. The detection parameters are over the 2θ range of 20^o to 90^o at a scan rate of 20^o min^{-1}, the voltage is 40 kV and the current is 40 mA. The thickness of corrosion products was detected by ZEISS GeminiSEM500 scanning electron microscope (SEM).

3. RESULTS AND DISCUSSION

3.1 Austenitic phase transformation of high Cr ferritic/martensitic steels upon different heating rates

Fig. 3 shows the thermal expansion curves of the high Cr ferritic/martensitic steel samples treated under different heating rates. It can be found that the shape and trend of the curve are independent of the heating rate. There are two typical endothermic characteristic peaks on each thermal expansion curve. A peak value is around 760 ^oC, which expresses the Curie temperature point of the high Cr ferritic/martensitic steel. The other peak value is in the temperature range of 830~980 ^oC, which represents the austenitic transformation (α′- matensite → γ- austenite) process of the high Cr ferritic/martensitic steel samples during continuous heating. Ac_1 is the onset temperature of austenitic transformation and Ac_3 is the finish temperature of austenitic transformation. It can be seen from the figure that with the increase of heating rate, the Curie temperature point hardly changes, while Ac_1 and Ac_3 increase, that is, the superheat degree of austenitic transformation increases significantly. This is because the austenitic transformation is a diffusional transformation, and its phase transformation rate is controlled by long-range atomic diffusion. Alloying elements such as Cr and W in steel increase the diffusion activation energy of C atoms in austenite and reduce the diffusion coefficient of C [27]. Moreover, strong carbide forming elements such as Ta, V and Cr have great affinity with C to form alloying carbides insoluble in austenite [28]. These carbides have stable structure and high melting point, which can delay the formation of austenite. In addition, the diffusion rate of alloying elements is very slow. As the heating rate increases, C and alloying elements do not diffuse at the equilibrium temperature, but push up the austenitic transformation temperature [29].

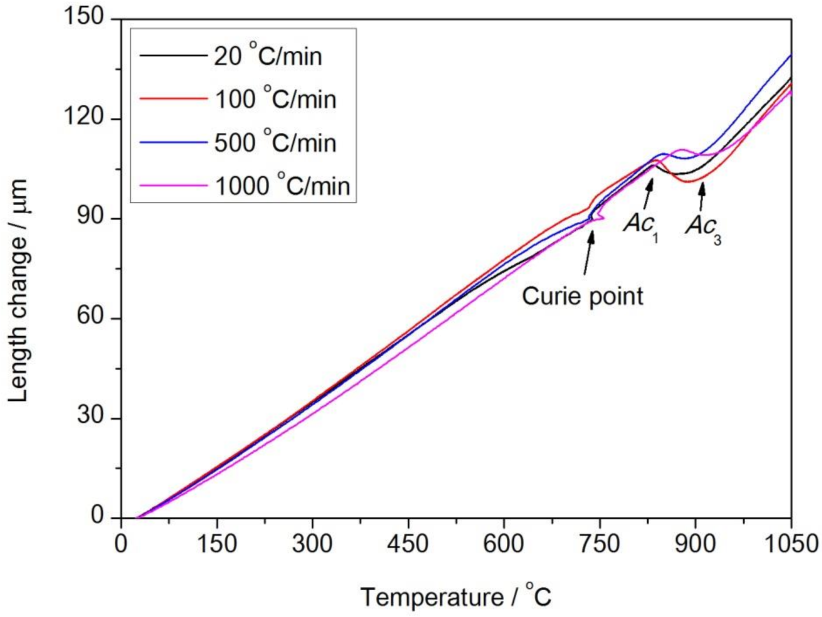

Figure 3. Thermal expansion curves of the high Cr ferritic/martensitic steel samples treated under different heating rates.

In order to accurately measure the change in austenitic transformation temperature, the tangent method was used to determine Ac_1 and Ac_3 [28]. The specific method is shown in Fig. 4. Table 2 shows the Ac_1 and Ac_3 values of high Cr ferritic/martensitic steels treated under different heating rates.

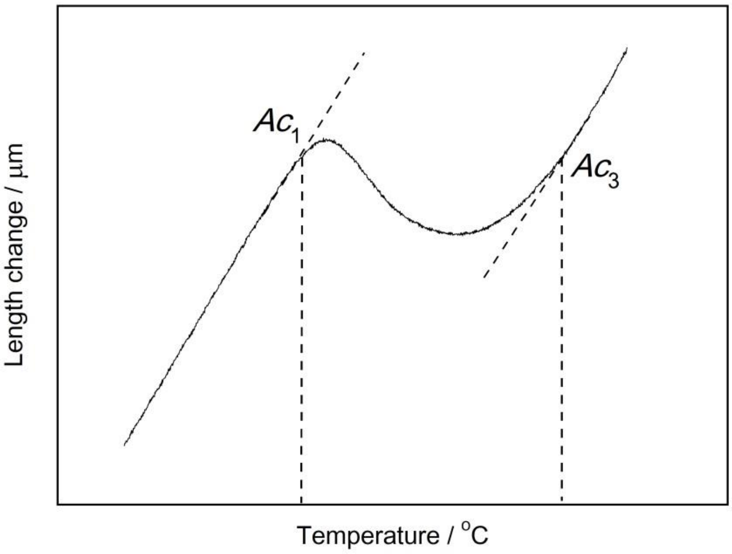

Figure 4. Tangent method used to measure the austenitic phase transformation temperature.

Table 2. Austenitic phase transformation temperatures of the high Cr ferritic/martensitic steel samples treated under different heating rates

Heating rates	Ac_1 (Onset temperature of austenitic transformation)	Ac_3 (Finish temperature of austenitic transformation)
20 °C/min	831	910
100 °C/min	835	928
500 °C/min	840	936
1000 °C/min	870	973

Fig. 5 shows the austenitic phase transformation time of high Cr ferritic/martensitic steel at different heating rates. The time required for austenite formation is determined by the following formula:

$$\Delta t=(Ac_3-Ac_1)/(dT/dt) \quad (1)$$

where dT/dt is the heating rate (°C/min).

It can be seen from the figure that the increase of heating rate shortens the austenitic transformation time, namely, the faster the heating rate is, the faster the austenitic formation rate is. This is because with the increase of heating rate, the austenitic transformation is delayed to a higher temperature and the superheat of phase transformation increases. Therefore, the nucleation and growth rate of phase transformation are accelerated, and the time required for austenite formation is reduced.

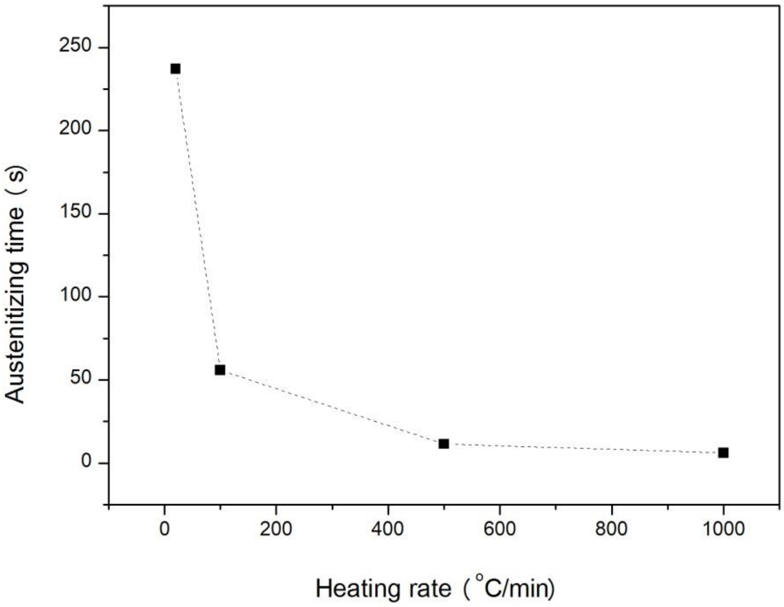

Figure 5. Austenitic phase transformation time of the high Cr ferritic/martensitic steel samples treated under different heating rates.

3.2 Microstructure of high Cr ferritic/martensitic steels upon different heating rates

3.2.1 OM observation

Fig. 6 shows the OM images of the high Cr ferritic/martensitic steel samples treated under different heating rates. It can be seen that the grains of samples obtained under different thermal simulation conditions are equiaxed. With the increase of heating rate, prior austenite grains show a refining trend. This is because with the increase of heating rate, the nucleation rate of austenite will increase and the prior austenite grains will become finer [31,32].

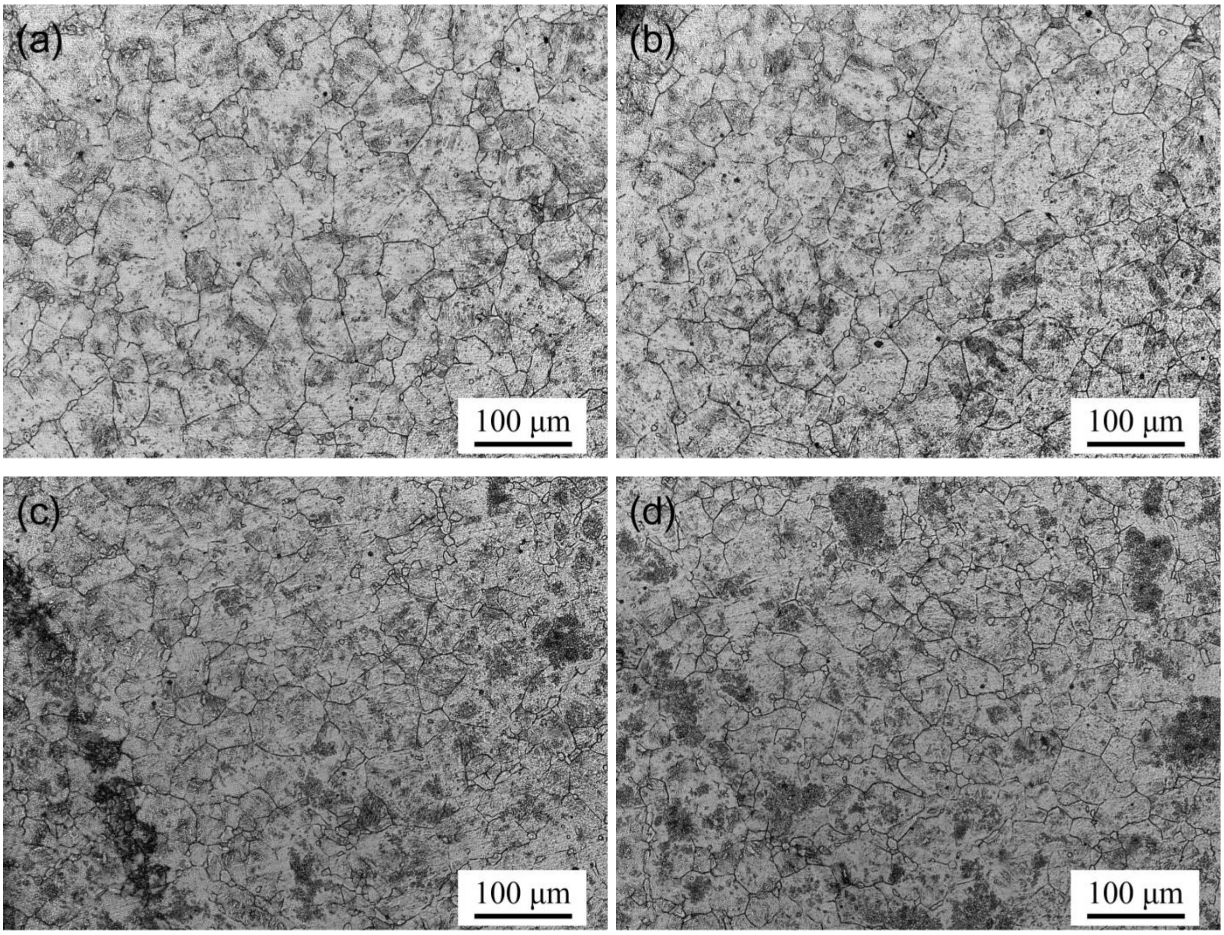

Figure 6. Optical micrographs of the high Cr ferritic/martensitic steel samples treated under different heating rates, (a) 20 °C/min, (b) 100 °C/min, (c) 500 °C/min, (d) 1000 °C/min.

Fig. 7 shows the statistical average values of prior austenite grain size obtained under different heating rates by measuring multiple OM images. It can be seen that as the heating rate increases from 20 °C/min to 1000 °C/min, the prior austenite grain size of the high Cr ferritic/martensitic steel decreases from 45 ± 4.7 µm to 34 ± 7.2 µm. This can be explained by the fact that when the heating rate is too fast, the second-phase particles are not completely dissolved, resulting in the pinning effect of the second-phases relative to austenite grain boundaries and hindering the growth of prior austenite grains [33]. When the heating rate is slow, the second-phase particles will be dissolved and redistributed, the effect of hindering the movement of grain boundaries will disappear, and the austenite grains will grow. In addition, when the heating rate is 1000 ºC/min, it can be seen from the error bar in Fig. 7 that the grain size is the most uneven, which is also due to the incomplete dissolution of second-phase particles, resulting in relatively fast grain growth in the dissolution zone of second-phases, while the grain growth around the undissolved second-phase is relatively slow.

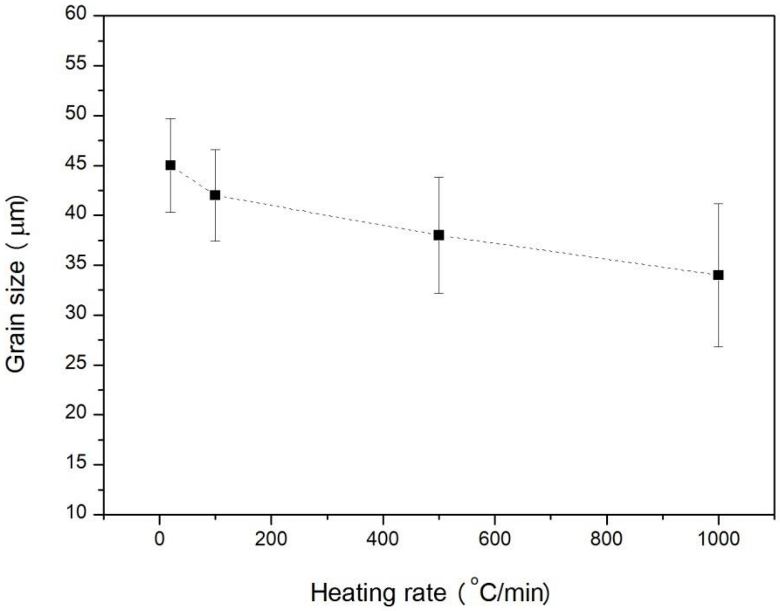

Figure 7. Austenite grain size of the high Cr ferritic/martensitic steel samples treated under different heating rates.

3.2.2 TEM observation

Fig. 8 shows the TEM images of carbon extraction replica samples of the high Cr ferritic/martensitic steels treated under different heating rates. The results show that the spherical and granular second-phases in the microstructure are linearly distributed, indicating that the second-phase particles are distributed along the prior austenite grain boundaries and lath boundaries. The distribution state of undissolved second-phase particles in carbon extraction replica samples under different thermal simulation conditions is significantly different. When the heating rate is relatively low (such as 20 ºC/min and 100 ºC/min), there is only a small amount of undissolved second-phases in the microstructure. The number of undissolved second-phases increases significantly with increasing heating rate. When the heating rate rises to 1000 ºC/min, there are more undissolved second-phases at the grain boundaries and lath boundaries. This is because as the heating rate increases, the austenitic transformation time is shortened, and the second-phases have no time to dissolve, therefore, there are some coarse insoluble second-phases. According to the EDS analysis in Fig. 8(e), it can be confirmed that the undissolved second-phase particles are mainly Cr rich carbide.

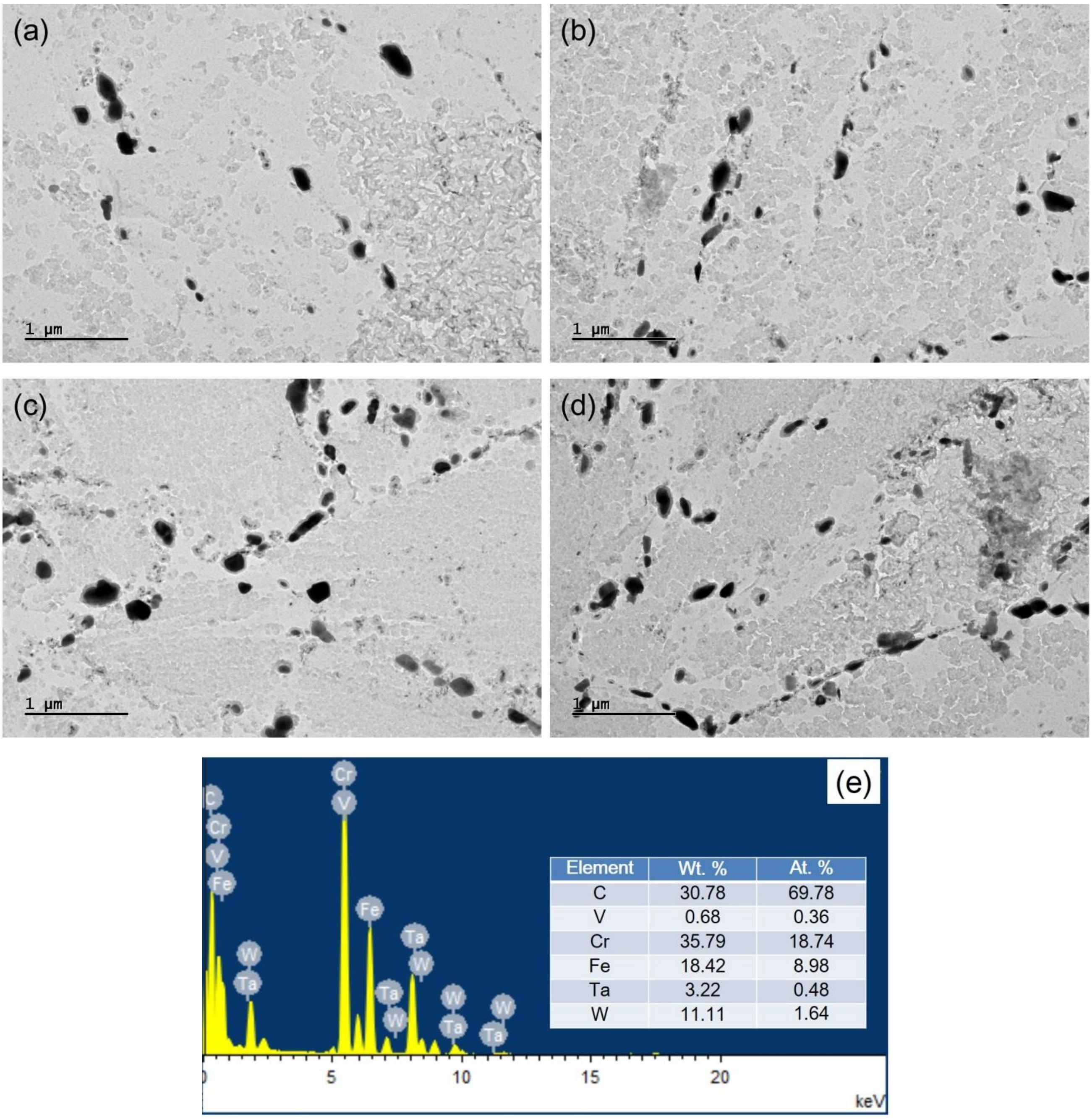

Element	Wt. %	At. %
C	30.78	69.78
V	0.68	0.36
Cr	35.79	18.74
Fe	18.42	8.98
Ta	3.22	0.48
W	11.11	1.64

Figure 8. TEM micrographs of extraction replica for the high Cr ferritic/martensitic steel samples treated under different heating rates, (a) 20 ^{o}C/min, (b) 100 ^{o}C/min, (c) 500 ^{o}C/min, (d) 1000 ^{o}C/min, (e) EDS analysis of carbide.

In order to quantify the distribution of undissolved carbides in high Cr ferritic/martensitic steels treated under different heating rates, Fig. 9 shows the quantitative size number statistical distribution of undissolved carbides in high Cr ferritic/martensitic steels treated under different heating rates. Each quantitative statistic is derived based on the statistics of multiple TEM images. It can be seen from the quantitative statistics chart that the number of carbides in the steel increases with the increase of heating rate, while the size of the carbides changes little with the increase of heating rate. This result is very consistent with the aforementioned grain size observation in the paper. In general, undissolved carbides are very effective in controlling grain growth by pinning grain boundaries during austenization [34-36]. When the heating rate is low, the alloying elements in the high Cr ferritic/martensitic steel dissolve relatively completely during the austenitizing process, the hindering effect on the growth of austenite grain is weakened, and the austenite grain size is large. However, when the heating rate is increased, the austenitic phase transformation time is too short and the second-phase particles are not completely dissolved, resulting in the enhancement of pinning effect on austenite grain boundaries and the reduction of austenite grain size.

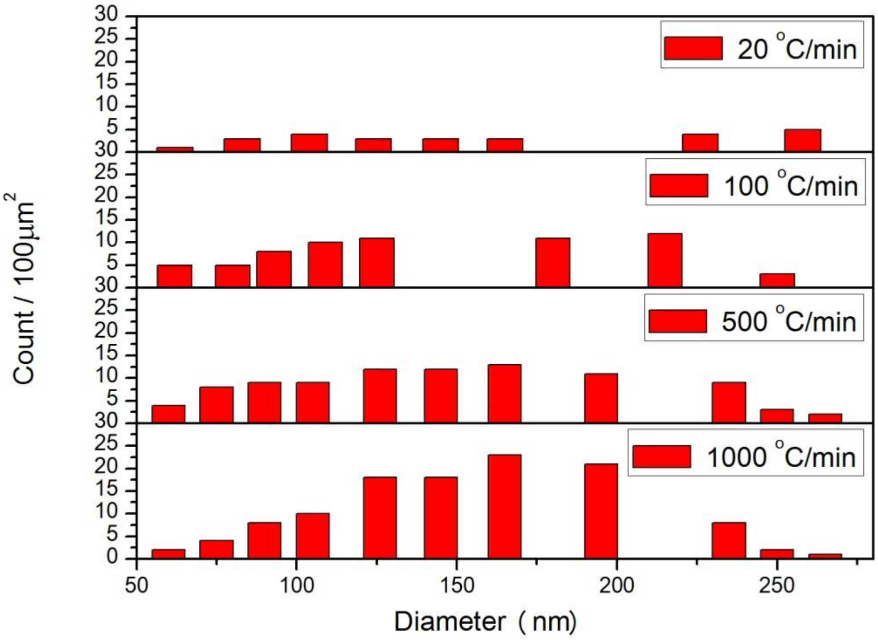

Figure 9. Number density of carbide in the high Cr ferritic/martensitic steel samples treated under different heating rates.

3.3 Corrosion behavior of high Cr ferritic/martensitic steels upon different heating rates

3.3.1 Electrochemical analysis

Fig. 10 shows the electrochemical polarization curves of the high Cr ferritic/martensitic steel samples as a function of heating rates in 3.5 wt.% NaCl solution. It can be seen that the shapes and changing trends of polarization curves for steel samples obtained under different heating rates are similar. This means that the corrosion mechanism of steel samples is the same. The corrosion current density (icorr) of each steel sample can be obtained by Tafel extrapolation of both the anodic and cathodic branches of the polarization curve [37]. Table 3 lists the corrosion potentials (Ecorr) and icorr of the high Cr ferritic/martensitic steel samples. From the data in the table, it can be found that with the increase of the heating rate, the icorr of the steel sample increases and the Ecorr decreases. The analysis of Ecorr and icorr shows that the corrosion resistance of the high Cr ferritic/martensitic steel decreases with the increase of heating rate.

Corrosion rate (in micrometers per year), the most direct parameters to evaluate the corrosion resistance of the high Cr ferritic/martensitic steels, can be expressed as follows [38]:

$$\text{Corrosion rate} = \frac{3.27 \times i_{corr} \times \mathrm{A}}{\mathrm{nD}} \qquad (2)$$

where A is the atomic quantity, n is the number of electrons exchanged in the electrochemical reaction, and D is the density of the metallic material. For Fe-based materials [39], A can be selected as the atomic quantity of iron (55.84), D can be chosen as the density of iron (7.90 g/cm^3), and the value of n is considered to be 2.

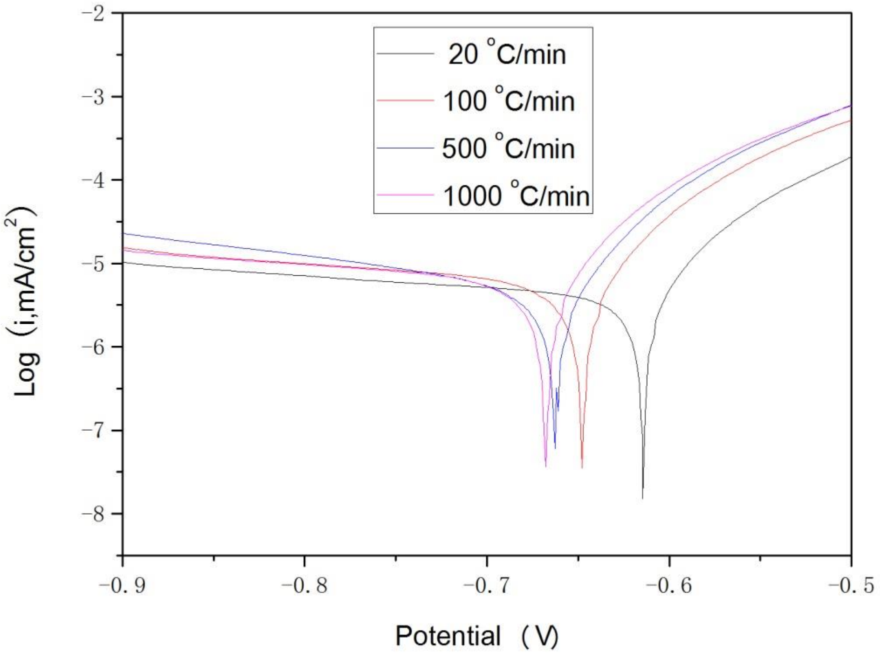

Figure 10. Potentiodynamic polarization curves of the high Cr ferritic/martensitic steel samples treated under different heating rates in 3.5 wt.% NaCl solution.

Table 3. Electrochemical parameters of the high Cr ferritic/martensitic steel samples treated under different heating rates in 3.5 wt.% NaCl solution

Heating Rate (°C/min)	E_{corr} (V)	I_{corr} (μA/cm^2)	Corrosion rate (μm/year)
20	-0.612	3.12	36.05
100	-0.646	3.48	40.22
500	-0.660	3.85	44.49
1000	-0.668	3.91	45.19

3.3.2 Corrosion products analysis

The corrosion products of the high Cr ferritic/martensitic steels treated under different heating rates immersed in 3.5 wt.% NaCl solution for 30 days were analyzed by XRD. The test results are shown in Fig. 11. It can be found that there is no difference in the phase composition of corrosion products as a function of heating rate. The corrosion products consist of iron hydroxide, specifically including α- FeOOH, β- FeOOH and γ- FeOOH. Among them, β- FeOOH and γ- FeOOH have strong reducibility and can promote the corrosion process [40].

The formation of corrosion products can be explained as follows [41]:

The steels are oxidized at the anode

$Fe \rightarrow Fe^{2+} + 2e$

The oxygen is reduced at the cathode

$O_2 + 2H_2O + 4e \rightarrow 4OH^-$

β- FeOOH and γ- FeOOH are formed by combining the reaction of anode and cathode

$2Fe + O_2 + 2H_2O \rightarrow 2Fe(OH)^+ + 2OH^-$

$2Fe(OH)^+ + 2OH^- + 1/2O_2 \rightarrow 2\beta\text{- }FeOOH + 2H_2O$

$2Fe(OH)^+ + 2OH^- + 1/2O_2 \rightarrow 2\gamma\text{- }FeOOH + 2H_2O$

Subsequently, as the corrosion progresses, the meta-stable phases (β- FeOOH and γ- FeOOH) will transform into the thermodynamically stable α- FeOOH phase [42].

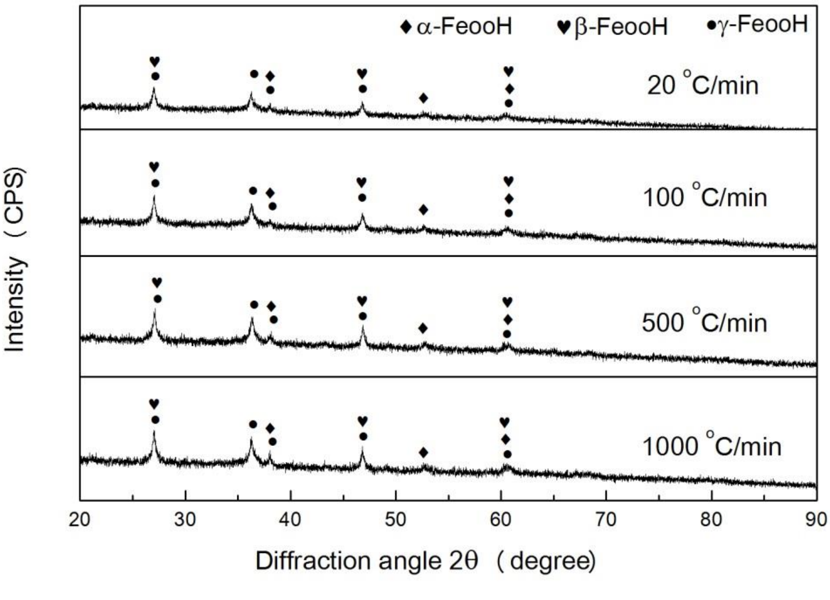

Figure 11. XRD phase analysis of corrosion products of the high Cr ferritic/martensitic steel samples treated under different heating rates corroded for 30 days in 3.5 wt.% NaCl solution

Fig. 12 shows the SEM images of the high Cr ferritic/martensitic steel samples treated under different heating rates after immersion in 3.5 wt.% NaCl solution for 30 days. It can be seen that as heating rate increases, the thickness of corrosion layer increases. At the same time, it is found that there are different degrees of potholes on the surface of the high Cr ferritic/martensitic steel. The higher the heating rate, the deeper the potholes of the corresponding sample, indicating the worse corrosion resistance, which is consistent with the electrochemical polarization curves test results. As the change of heating rate, the steel changes in two aspects: one is the decrease of grain size, and the other is the increase of carbides at grain boundaries and lath boundaries, as shown in Fig.6 - Fig.9.

3.3.3 Corrosion mechanism analysis

The reason for the change of corrosion resistance of the high Cr ferritic/martensitic steel samples treated under different heating rates can be explained as follows:

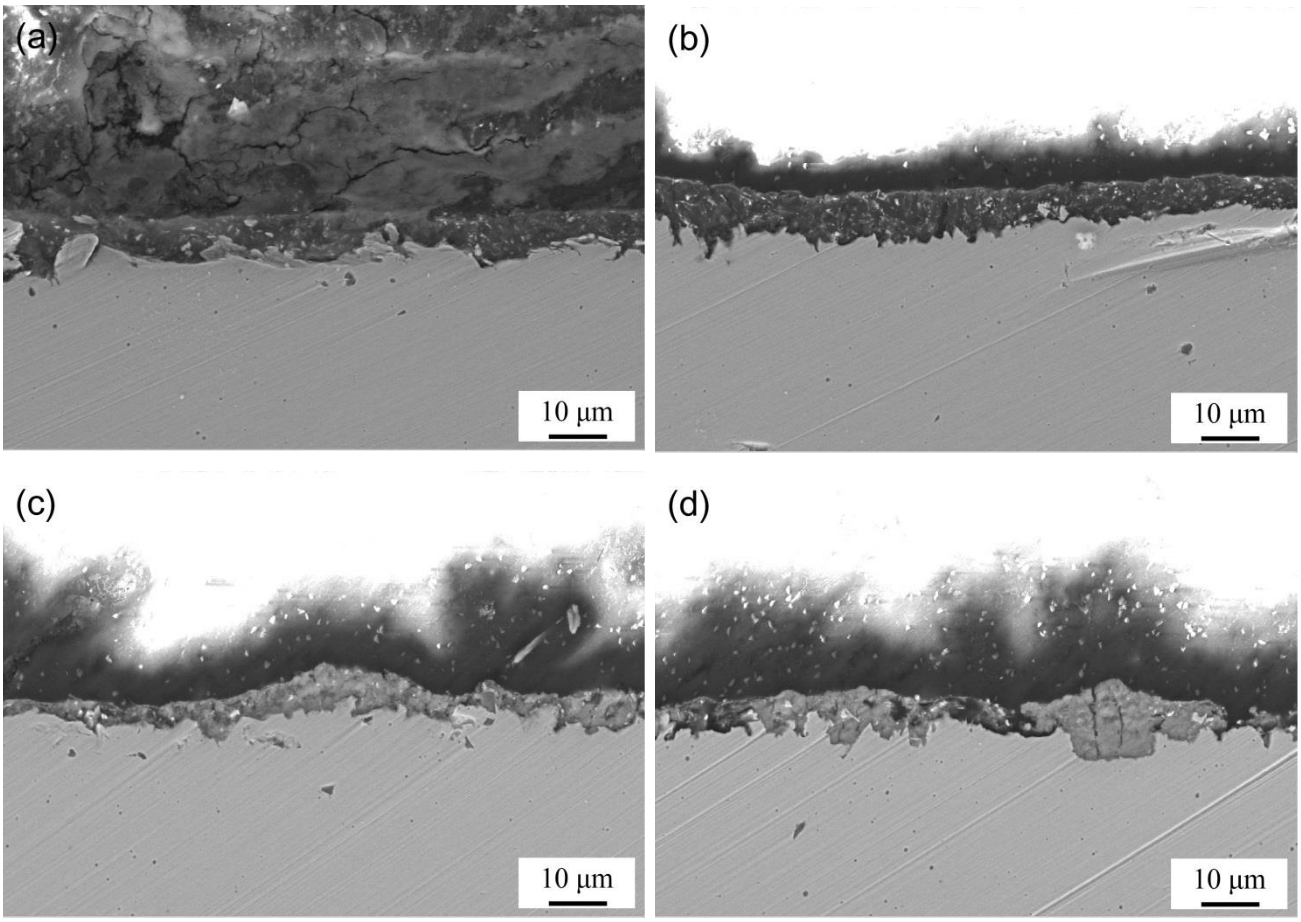

Figure 12. SEM micrographs of the high Cr ferritic/martensitic steel samples treated under different heating rates after 30 days in 3.5 wt.% NaCl solution, (a) 20 $^oC/min$, (b) 100 $^oC/min$, (c) 500 $^oC/min$, (d) 1000 $^oC/min$.

Firstly, there is a phase potential difference between the Cr rich carbide and the matrix, which will form a local galvanic couple [43]. Secondly, the Cr rich carbide second-phases segregated at the grain boundaries and lath boundaries are difficult to dissolve at high heating rate. A large amount of Cr rich carbides decorated along the grain boundaries and lath boundaries will lead to Cr depletion at its adjacent boundaries and degrade the corrosion resistance of the grain boundaries and lath boundaries

[44-46]. Thirdly, a higher density of boundaries obtained at high heating rate will increase the probability of Cr depletion at adjacent carbide sites. These will increase the tendency of the high Cr ferritic/martensitic steel to develop pitting corrosion, and then promote the occurrence of corrosion.

4. CONCLUSIONS

In this work, the effects of heating rate on austenitic transformation and corrosion property of high Cr ferritic/martensitic steel have been studied. The following conclusions can be drawn:

(1) The onset temperature of austenitic transformation and the finish temperature of austenitic transformation increase with the increase of heating rate.

(2) The austenitic transformation time of the high Cr ferritic/martensitic steel decreases with the increase of heating rate.

(3) With the increase of heating rate, the prior austenite grain size of the high Cr ferritic/martensitic steel decreases, while the amount of undissolved carbide at grain boundaries and lath boundaries increases.

(4) The corrosion current density of the high Cr ferritic/martensitic steel increases and the corrosion resistance decrease with the increase of heating rate.

ACKNOWLEDGEMENTS
This work was financially supported by the Science and Technology Support Key Projects of Tianjin Key R&D Program (No. 20YFZCGX00480), Science and Technique Plan Project of State Administration for Market Regulation (No. 2021MK015), and the Science and Technology Program of Tianjin Administration for Market Regulation (No. 2021-W06). Thanks to partial support for this work from National Detection and Inspection Center for Special Equipment Welding Consumables Quality (Tianjin).

CONFLICTS OF INTEREST
The authors declare that they have no known competing financial interests that could have appeared to influence the work reported in this paper.

References

1. X. Zhou, C. Liu, L. Yu, Y. Liu and H. Li, *J. Mater. Sci. Technol.*, 31 (2015) 235. https://doi.org/10.1016/j.jmst.2014.12.001
2. J.G. Chen, Y.C. Liu, Y.T. Xiao, Y.H. Liu, C.X. Liu and H.J. Li, *Acta Metall. Sin. (Engl. Lett.)*, 31 (2018) 706. https://doi.org/10.1007/s40195-018-0703-y
3. X. Zhou, Y. Liu, C. Liu and B. Ning, *Mater. Sci. Eng.* A 608 (2014) 46. https://doi.org/10.1016/j.msea.2014.04.075
4. H. He, L. Yu, C. Liu, H. Li, Q. Gao and Y. Liu, *Acta Metall. Sin.*, 58 (2022) 311. https://doi.org/ 10.11900/0412.1961.2021.00185
5. J.G. Chen, C.X. Liu, C. Wei, Y.C. Liu and H.J. Li, *Acta Metall. Sin. (Engl. Lett.)*, 32 (2019) 1151. https://doi.org/ 10.1007/s40195-019-00883-6

6. Z. Liu, X.J. Huo, Y.H. Yu, C. Zhang, N. Xiao, J.L. Zhao and Z.G. Yang, *Mater. Sci. Eng.* A, 826 (2021) 141934.
https://doi.org/ 10.1016/j.msea.2021.141934
7. X.S. Zhou, Y.C. Liu, C.X. Liu, L.M. Yu and H.J. Li, *Metall. Mater. Trans.* A, 49 (2018) 3525.
https://doi.org/10.1007/s11661-018-4723-z
8. J.G. Chen, C.X. Liu, Y.C. Liu, B.Y. Yan and H.J. Li, *J. Nucl. Mater.*, 479 (2016) 295.
https://doi.org/10.1016/j.jnucmat.2016.07.029
9. B. Białobrzeska, Ł. Konat and R. Jasiński, *Metals*, 7 (2017) 26.
https://doi.org/10.3390/met7010026
10. Z.X. Xia, J.C. Xu, J.J. Shi, T. Shi, C.F. Sun and D. Qiu, *Addit. Manuf.*, 33 (2020) 101114.
https://doi.org/10.1016/j.addma.2020.101114
11. M. Militzer, E.B. Hawbolt, T. Ray Meadowcroft and A. Giumelli, *Metall. Mater. Trans.* A, 27 (1996) 3399.
https://doi.org/10.1007/BF02595433
12. Y. Shao, B.Y. Yan, Y.H. Liu, C.L. Mao, C. Wei, Y.C. Liu, Z.S. Yan, H.J. Li and C.X. Liu, *J Manuf. Process.*, 43 (2019) 9.
https://doi.org/10.1016/j.jmapro.2019.05.012
13. L. Tan, D.T. Hoelzer, J.T. Busby and R.L. Klueh, *J. Nucl. Mater.*, 422 (2012) 45.
https://doi.org/10.1016/j.jnucmat.2011.12.011
14. F. Abe, M. Tabuchi, *Sci. Technol. Weld. Joi.*, 9(2013) 22.
https://doi.org/10.1179/136217104225017107
15. N. Saini, R. Raghav, V. Bist, R.S. Mulik and M.M. Mahapatra, *Int. J. Pres. Ves. Pip.*, 194 (2021) 104556.
https://doi.org/10.1016/j.ijpvp.2021.104556
16. Q. Zhu, Y.C. Lei, X.Z. Chen, W.J. Ren, X. Ju and Y.M. Ye, *Fusion Eng. Des.*, 86 (2011) 407.
https://doi.org/10.1016/j.fusengdes.2011.03.070
17. C.R. Das, S.K Albert, Shiju Sam, P. Mastanaiah, G.M.S.K. Chaitanya, A.K. Bhaduri, T. Jayakumar, C.V.S. Murthy and E. Rajendra Kumar, *Fusion Eng. Des.*, 89 (2014) 2672.
https://doi.org/10.1016/j.fusengdes.2014.07.001
18. Hemant Kumar, K.V. Phani Prabhakar, Shiju Sam, S.K. Albert, G. Padmanabham, A.K. Bhaduri, T. Jayakumar and E. Rajendra Kumar, *Fusion Sci. Technol.*, 66 (2014) 192.
https://doi.org/10.13182/FST13-747
19. A. Karmakar, S. Kundu, S. Roy, S. Neogy, D. Srivastava and D. Chakrabarti, *Mater. Sci. Technol.*, 30 (2014) 653.
https://doi.org/10.1179/1743284713Y.0000000386
20. H. Ma, S.L. Liao and S.F. Wang, *J. Iron Steel Res. Int.*, 21 (2014) 702.
https://doi.org/10.1016/S1006-706X(14)60109-6
21. C. Wei, Z.J. Wang and J.G. Chen, *Eng. Fail. Anal.*, 135 (2022) 106111.
https://doi.org/10.1016/j.engfailanal.2022.106111
22. Y.C. Liu, F. Sommer and E.J Mittemeijer, *Acta Mater.*, 51 (2003) 507.
https://doi.org/10.1016/S1359-6454(02)00434-2
23. Y.C. Liu, F. Sommer and E.J Mittemeijer, *Acta Mater.*, 57 (2009) 2858.
https://doi.org/10.1016/j.actamat.2009.02.044
24. Y.C. Liu, F. Sommer and E.J Mittemeijer, *Acta Mater.*, 58 (2010) 753.
https://doi.org/10.1016/j.actamat.2009.09.048
25. Y.C. Liu, D.J. Wang, F. Sommer and E.J Mittemeijer, *Acta Mater.*, 56 (2008) 3833.
https://doi.org/10.1016/j.actamat.2008.04.015
26. J.G. Chen, Y.C. Liu, C.X. Liu, X.S. Zhou and H.J. Li, *J. Mater. Res.*, 32 (2013) 1376.
https://doi.org/10.1557/jmr.2017.77
27. L. Kong, Y. Liu, J. Liu, Y. Song, S. Li, R. Zhang, T. Li and Y. Liang, *J. Alloy. Compd.*, 648 (2015)

494.
https://doi.org/10.1016/j.jallcom.2015.06.259

28. J.G. Chen, Y.C. Liu, C.X. Liu, B.Y. Yan and H.J. Li, *J. Iron Steel Res. Int.*, 24 (2017) 705. https://doi.org/10.1016/s1006-706x(17)30106-1
29. C.X. Liu, Y.C. Liu, D.T. Zhang and Z.S. Yan, *Appl. Phys.* A, 105 (2011) 949. https://doi.org/10.1007/s00339-011-6517-7
30. Q.J. Ma, Y. Shao, Y.C. Liu, Z.M. Gao and L.M. Yu, *Int. J. Mater. Res.*, 104 (2013) 935. https://doi.org/10.3139/146.110951
31. S. Morito, H. Saito, T. Ogawa, T. Furuhara and T. Maki, *ISIJ. Int.*, 45 (2005) 91. https://doi.org/10.2355/isijinternational.45.91
32. S. Morito, H. Yoshida, T. Maki and X. Huang, *Mater. Sci. Eng.* A 438 (2006) 237. https://doi.org/10.1016/j.msea.2005.12.048
33. S. Maropoulos, S. Karagiannis and N. Ridley, *Mater. Sci. Eng.* A 483 (2008) 735. https://doi.org/10.1016/j.msea.2006.11.172
34. Z. Xia, C. Zhang, H. Lan and Z. Yang, *J. Mater. Sci.*, 46 (2011) 3151. https://doi.org/10.1007/s10853-010-5196-7
35. Z. Xia, C. Zhang, Q. Huang, S. Liu, Z. Li and Z. Yang, *J. Iron Steel Res. Int.*, 18 (2011) 47. https://doi.org/10.1016/S1006-706X(12)60033-8
36. X. Zhou, G. Liu, X. Shen and Y. Liu, *Mater. Sci. Eng.* A, 829 (2022) 142071. https://doi.org/ 10.1016/j.msea.2021.142071
37. C. Wei, Y.S. Wei, Z.J. Wang and J.G. Chen, *Int. J. Electrochem. Sci.*, 17 (2022) 220622. https://doi.org/10.20964/2022.06.02
38. D.Song, J. Hao, F. Yang, H. Chen, N. Liang, Y. Wu, J. Zhang, H. Ma, E.E. Klu, B. Gao, Y. Qiao, J. Sun and J. Jiang, *J. Alloy. Compd.*, 809 (2019) 151787. https://doi.org/10.1016/j.jallcom.2019.151787
39. J.G. Chen, Y.M. Yang, L.Q. Li, Z.J. Wang, H.Y. Xiao, Y.S. Wei, T.H. Zhu and H. Song, *Int. J. Electrochem. Sci.*, 16 (2021) 210825. https://doi.org/10.20964/2021.08.36
40. H. Antony, S. Perrin, P. Dillmann, L. Legrand and A. Chaussé, *Electrochim. Acta*, 52 (2007) 7754. https://doi.org/10.1016/j.electacta.2007.04.029
41. Y. Zhou, J. Chen and Z. Liu, *J. Iron Steel Res. Int.*, 20 (2013) 66. https://doi.org/10.1016/S1006-706X(13)60071-0
42. Sei J. Oh, D.C. Cook and H.E. Townsend, *Corros. Sci.*, 41 (1999) 1687. https://doi.org/10.1016/S0010-938X(99)00005-0
43. H. Wan, Y. Cai, D. Song and C. Chen, *Corros. Sci.*, 167 (2020) 108518. https://doi.org/10.1016/j.corsci.2020.108518
44. S. Zhang, H. Li, Z. Jiang, B. Zhang, Z. Li, J. Wu, S. Fan, H. Feng and H. Zhu, *Mater. Charact.*, 152 (2019) 141. https://doi.org/10.1016/j.matchar.2019.04.010
45. S. Hu, Y. Mao, X. Liu, E. Han and H. Hänninen, *Corros. Sci.*, 166 (2020) 108420. https://doi.org/10.1016/j.corsci.2019.108420
46. X.L. Li, L.T. Chang, C.P. Liu, B. Leng, X.X. Ye, F.F. Han and X.M. Yang, *Corros. Sci.*, 191 (2021) 109784. https://doi.org/10.1016/j.corsci.2021.109784